Polymer 50 (2009) 4876–4887

Contents lists available at ScienceDirect

Polymer

journal homepage: www.elsevier.com/locate/polymer

Influence of octakis-functionalized polyhedral oligomeric silsesquioxanes on the physical properties of their polymer nanocomposites

Kai-Wei Huang, Li-Wei Tsai, Shiao-Wei Kuo*

Department of Materials and Optoelectronic Science, Center for Nanoscience and Nanotechnology, National Sun Yat-Sen University, Kaohsiung 804, Taiwan

ARTICLE INFO

Article history:
Received 6 May 2009
Received in revised form
9 August 2009
Accepted 14 August 2009
Available online 20 August 2009

Keywords:
POSS
Nanoparticles
Miscibility

ABSTRACT

We synthesized the polyhedral oligomeric silsesquioxane (POSS) derivatives octakis[dimethyl(phenethyl)siloxy]silsesquioxane (OS-POSS), octakis[dimethyl(4-acetoxy phenethyl)siloxy]silsesquioxane (OA-POSS), and octakis[dimethyl(4-hydroxyphenethyl)siloxy] silsesquioxane (OP-POSS) through hydrosilylation with octakis(dimethylsiloxy)silsesquioxane ($Q_8M_8^H$). To investigate the influence of these octuply functionalized POSS derivatives in polymer nanocomposites, we blended OP-POSS, OA-POSS, and OP-POSS with the homopolymer poly(ethylene oxide) (PEO) and characterized its resulting intermolecular interactions (e.g., hydroxyl–ether and carbonyl–ethylene oxide) using FTIR spectroscopy. The thermal properties of these blend systems were investigated using differential scanning calorimetry (DSC) and dynamic mechanical analysis (DMA). The crystallization kinetics in the miscible binary blends of the crystalline polymer and these inorganic nanoparticles were also determined through DSC and optical microscopy (OM) analyses. Herein, we emphasize the effects of the functional groups on POSS nanocomposites on the crystallization kinetics of PEO. We found that OP-POSS/PEO blend had the highest thermal stability and lowest crystallization rate because its hydrogen bonding interactions (between its hydroxyl and ether units) were stronger than those (between carbonyl and methylene groups) in OA-POSS/PEO.

1. Introduction

Nanocomposite materials, because of the length scales involved, feature extensive number of interfacial interactions that can result in salient changes in their properties. When developing polymer nanocomposites, the attachment of organic groups to nanosized materials can have wide-ranging implications on the interactions occurring at the interfaces between the inorganic composite particles and the organic polymer matrices [1–3]. Recently, a novel class of organic/inorganic hybrid materials based on polyhedral oligomeric silsesquioxane (POSS) and possessing well-defined chemical structures have been developed through co-polymerization of POSS co-monomer units [4–15] having the general formula $(RSiO_{1.5})_8$, where the R units are organic groups located at the corners of octahedral siloxane cubes $(SiO_{1.5})_8$ [16–21]. The synthesis of a random copolymer is, however, generally more complicated and time-consuming than the preparation of a physical blend; therefore, polymer blending is seen as a more convenient method of preparing polymer/POSS nanocomposites [22–24]. Nevertheless, most inorganic silicas or creamers are immiscible in most general organic systems because of poor specific interactions in these organic/inorganic hybrids. To improve the properties and miscibility of hybrid materials, it is usually necessary to ensure that favorable specific interactions exist between these components, such as hydrogen bonding, dipole–dipole interactions, and acid/base complexation.

In previous studies, we found that polymer–POSS nanocomposites prepared through blending exhibited enhanced thermal properties [25,26], but we did not clearly identify the effects that the functional groups on the POSS derivatives had on the behavior of the polymer nanocomposites. Wu et al. reported that polystyrene (PS)-based random copolymers incorporating POSS units featuring three types of vertex group (isobutyl, cyclopentyl, and cyclohexyl) exhibited differences in their glass transition temperatures (T_g) because of the different types of interactions of these three groups with the copolymers [27]. In this study, we performed the hydrosilylation of unsaturated monomers using octakis(dimethylsiloxy)silsesquioxane $Q_8M_8^H$ and Karstedt's catalyst (a platinum divinylsiloxane complex) to yield various POSS derivatives possessing distinct functionalities, including hydroxyl [28,29], poly(ethylene glycol) [30–32], liquid crystal mesogen [16,33], epoxy [34], and phenol [35] units. Although much literature

* Corresponding author. Tel.: +886 7 5252000x4079; fax: +886 7 5254099.
E-mail address: kuosw@faculty.nsysu.edu.tw (S.-W. Kuo).

0032-3861/$ – see front matter © 2009 Elsevier Ltd. All rights reserved.
doi:10.1016/j.polymer.2009.08.026

is available highlighting the excellent performance of hydrosilylated POSS-based polymer nanocomposites, few reports have focused on the effects of functional groups on their properties. In previous studies of POSS-based nanocomposites [23,24,26], we synthesized and characterized three amorphous POSS derivatives (Scheme 1): octakis[dimethyl(phenethyl)siloxy] silsesquioxane (OS-POSS), octakis[dimethyl(4-acetoxy phenethyl)siloxy]silsesquioxane (OA-POSS), and octakis[dimethyl(4-hydroxyphenethyl)siloxy]silsesquioxane (OP-POSS).

Poly(ethylene oxide) (PEO) is a highly crystalline polymer that is miscible with several amorphous polymers—including phenoxy [36], poly(acrylic acid) [37], poly(vinyl alcohol) [38], poly(vinyl phenol) [39], and phenolic resin [40]—as a result of the formation of strong hydrogen bonds. In addition, blends of PEO with many weakly interacting polymers—including poly(acetoxystyrene) [41], poly(methyl methacrylate) (PMMA) [42], poly(vinyl acetate) [43], and poly(vinyl pyrrolidone) [44]—are also fully miscible. From the chemical structures of OP-POSS, OA-POSS, and OS-POSS, we expected that OP-POSS and OA-POSS would form miscible amorphous phases with PEO through strong and weak hydrogen bonding interactions, respectively, but that PEO would be immiscible with OS-POSS because no specific interactions occur between styrene and ethylene oxide units. Therefore, we suspected that the influence that the functional groups on the POSS nanocomposites would have on the polymer matrix would be readily discernable through simple blending.

In this study, we used differential scanning calorimetry (DSC), thermogravimetric analysis (TGA), and dynamic mechanical analysis (DMA) to determine the thermal decomposition temperatures, char yields, and glass transition temperatures, respectively, of amorphous POSS-based nanocomposites. 1D and 2D Fourier transform infrared (FTIR) spectroscopy provided evidence for specific intermolecular association between the functional groups of POSS and PEO. The generalized two-dimensional (2D) correlation spectroscopy proposed by Noda has been applied widely in polymer science in recent years [45,46]. This novel method treats spectral fluctuations as a function of time, temperature, pressure, and composition to investigate specific interactions between polymer chains. In this study, we use generalized 2D IR correlation spectroscopy to explore the weak hydrogen bonding interactions in blends of PEO and OA-POSS, which are similar to those in poly(acetoxystyrene)/PEO blend [41]. In addition, we also determined the crystallization kinetics in miscible binary blends of crystalline polymers with inorganic nanoparticles using DSC and optical microscopy (OM). In this paper, we emphasize the effects that the functional groups of the POSS nanocomposites have on the crystallization kinetics relative to that of pure PEO.

2. Experimental section

2.1. Materials

$Q_8M_8^H$ POSS was obtained from Hybrid Plastics. 4-Acetoxystyrene (96%), styrene, hydrazine monohydrate (98%), platinum(0)/1,3-divinyl-1,1,3,3-tetramethyldisiloxane complex solution [Pt(dvs)] in xylene (Pt content = ca. 2%), and PEO (M_n = 20,000 g/mol) were obtained from Aldrich Chemical (USA).

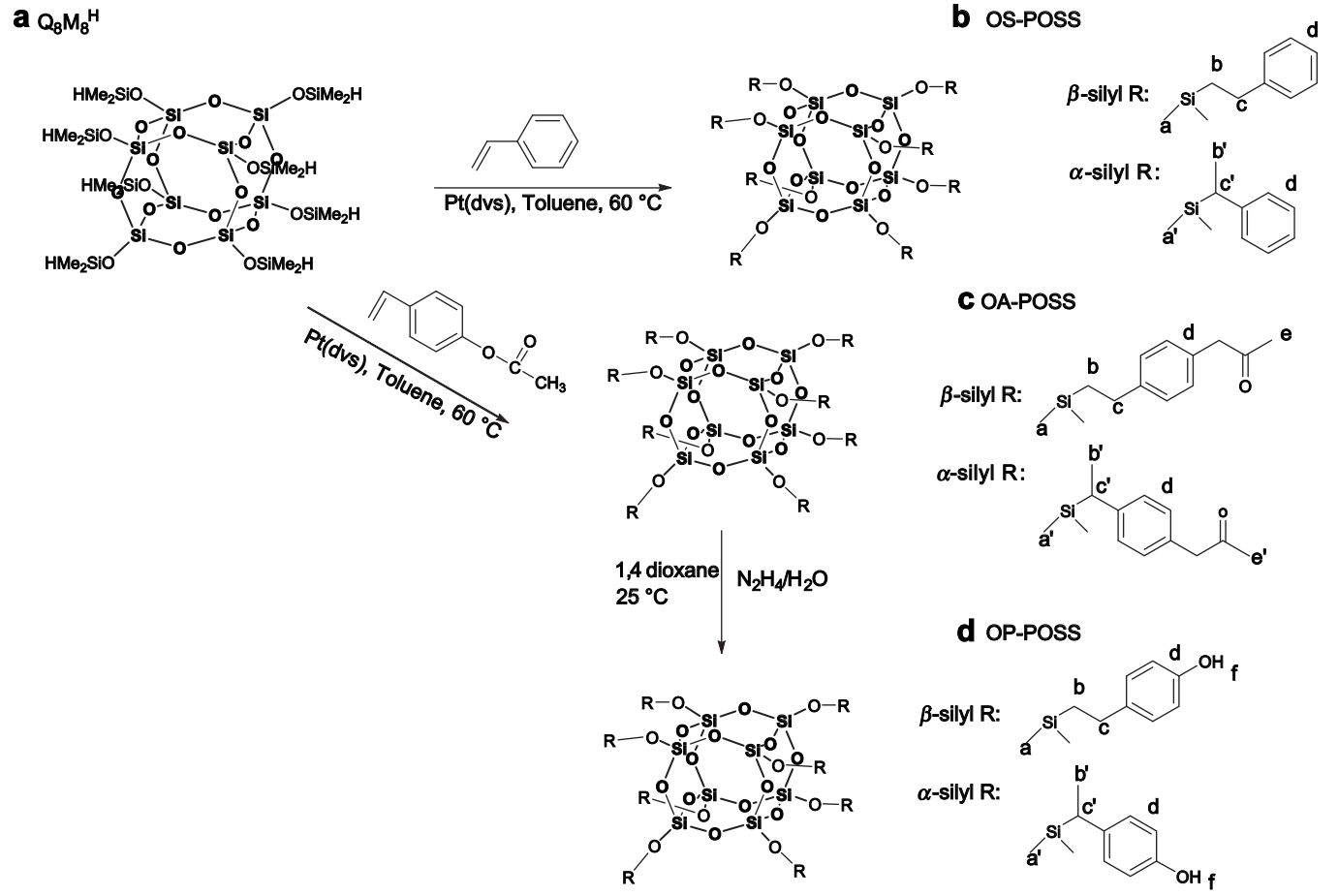

Scheme 1. Hydrosilylation and chemical structures of styrenic monomers with $Q_8M_8^H$ to give OS-POSS, OA-POSS and OP-POSS.

2.2. OS-POSS and OA-POSS

Scheme 1 depicts the hydrosilylation approach used to prepare OS-POSS and OA-POSS [26]. In a 100 mL Schlenk flask equipped with a reflux condenser and a magnetic stirrer, a solution of $Q_8M_8^H$ (3.00 g, 2.95 mmol) and styrene (2.46 g, 23.57 mmol) or 4-acetoxystyrene (3.98 g, 23.57 mmol) in toluene (30 mL) was heated at 60 °C under argon and then Pt(dvs) (0.2 mL, 0.4 μmol) was added via syringe. The reaction, which was monitored by measuring the decrease in intensity of the FTIR spectral signal at 2134 cm^{-1} for the Si–H bonds, was complete after 4 h. The yellowish, transparent reaction mixture became clear after removal of the Pt(dvs) catalyst through flash chromatography (neutral Al_2O_3; toluene). After evaporating the solvent under reduced pressure, the residual styrene or 4-acetoxystyrene was vacuum-distilled (80 °C, 0.2 Torr) to yield OS-POSS (3.45 g, 63%) or OA-POSS (3.93 g, 56%). OS-POSS is a fluid liquid at 25 °C; OA-POSS is a viscous liquid at 25 °C. Both are soluble in common organic solvents, such as tetrahydrofuran, chloroform, and acetone.

2.3. OP-POSS

Scheme 2 depicts the acetoxyl hydrazinolysis of OA-POSS with hydrazine monohydrate used to prepare OP-POSS [30]. Hydrazine monohydrate (1.73 g, 34.6 mmol, 16.0 equiv.) was added to a solution of OA-POSS (5.00 g, 2.16 mmol) in 1,4-dioxane. The acetoxyl hydrazinolysis, which was monitored by measuring the decrease in intensity of the FTIR spectral signal for the C=O bond at 1762 cm^{-1}, was complete after 2 h. The solution was then added dropwise into excess deionized water. The viscous OP-POSS was collected in a beaker, dissolved in EtOAc, dried (anhydrous $MgSO_4$), and filtered. The solvents were evaporated under vacuum at 80 °C for 4 h to yield OP-POSS (3.72 g, 87%), which is highly viscous (as a result of hydrogen bonding between the phenol units) and soluble in polar organic solvents (e.g., methanol).

2.4. Blend preparation

Blends of PEO and the functionalized POSS derivatives were prepared at various compositions through solution blending. A THF solution containing 5 wt% of the mixture was stirred for 6–8 h and then the solvent was evaporated slowly at room temperature over 1 day. To ensure total removal of solvent, the powder of the blend obtained was dried in a vacuum oven at 60 °C for 2 days.

2.5. Characterization

Using $CDCl_3$ as the solvent, ^1H NMR spectra were recorded on a Varian Unity Inova 500 FT NMR spectrometer operated at 500 MHz; chemical shifts are reported in parts per million (ppm). A Biflex III (Bruker Daltonics) time-of-flight mass spectrometer equipped with a 337 nm nitrogen laser was used to record MALDI-TOF mass spectra of the samples. The glass transition and melting temperatures of the blend films were determined through DSC using a TA Q-20 instrument. The scan rate was 20 °C/min within the temperature range 30–100 °C; the temperature was then held at 100 °C for 3 min to ensure complete removal of residual solvent. Glass transition temperatures were measured in the DSC sample cell after the sample (5–10 mg) had been cooled 20 °C/min to −90 °C from the melt of the first scan. The value of T_g was defined at the midpoint of the heat capacity transition between the upper and lower points of deviation from the extrapolated liquid and glass lines. DSC was also employed to study the kinetics of isothermal crystallization by rapid cooling to the crystallization temperature (T_c) from the melt at 80 °C for 10 min, and then maintaining the sample at T_c for 12 h. The crystallinity is expressed as the ratio of the peak area at time t to that at the end of crystallization. After the isothermal crystallization was completed, the sample was cooled to 0 °C and then heated to 100 °C at a heating rate of 10 °C/min to measure the melting temperature (T_m). A TA Instruments thermogravimetric analyzer Q50 (scan rate: 20 °C; from 30 to 800 °C; nitrogen purge: 40 mL/min) was used to record TGA thermograms of the samples positioned on a platinum holder. DMA was performed using a Perkin–Elmer Instruments DMA 8000 apparatus operated in tension mode over a temperature range from −150 to 100 °C. Analyses of the loss tangent (tan δ) were recorded automatically by the system. The heating rate and frequency were fixed at 2 °C/min and 1 Hz, respectively. FTIR spectra of the polymer blend films were recorded using the conventional KBr disk method. A THF solution containing the blend was cast onto a KBr disk and dried under conditions similar to those used in the bulk preparation. The film used in this study was sufficiently thin to obey the Beer–Lambert law. FTIR spectra were recorded using a Bruker Tensor 27 FT-IR spectrophotometer; 32 scans were collected at a spectral resolution 1 cm^{-1}. Because polymers containing OH groups are hygroscopic, pure N_2 gas was used to purge the spectrometer's optical box to maintain the sample films' dryness. Generalized 2D correlation analysis was performed using the 2D Shige software developed by Shigeaki Morita (Kwansei-Gakuin University, Japan). In the 2D correlation maps, white-colored regions are defined as positive correlation intensities; shaded regions are defined as negative correlation intensities.

The spherulite growth rate was determined using an Olympus polarized light microscope (Japan) equipped with a Mettler FP90 heating stage and photographed with a CCD camera. Each sample was sandwiched between two thin glass slides, melted for 10 min on a hot stage at 80 °C, and then transferred as quickly as possible onto another hot stage preheated to the desired value of T_c. The samples were crystallized isothermally at a given value of T_c to monitor the growth of the spherulite as a function of time. The

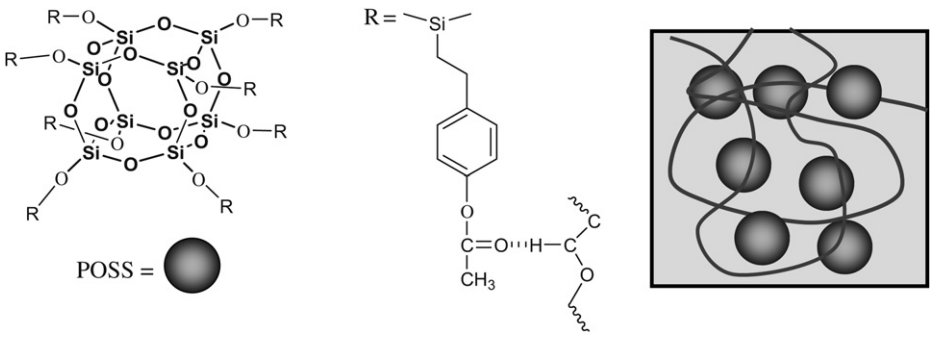

Scheme 2. C=O groups of OA-POSS interacted with the CH_2 segments of PEO.

radial growth rate of the PEO spherulite was calculated from the slope of the line obtained from a plot of the spherulitic radius versus time.

3. Results and discussion

3.1. Syntheses of POSS derivatives

At 1:8 molar ratios of $Q_8M_8^H$ to the vinyl monomers, the hydrosilylations yielding OS-POSS and OA-POSS [Scheme 1(a) and (b), respectively] were complete after 4 h, as adjudged by monitoring the disappearance of the signals of the Si–H groups (FTIR: 2134 cm^{-1}; ^1H NMR: 4.7 ppm) in the reaction mixtures. OS-POSS and OA-POSS were purified through evaporation of the residual volatile styrene and 4-acetoxystyrene, respectively, under vacuum. The acetoxyl hydrazinolysis [Scheme 1(d)] with hydrazine monohydrate can be used to selectively deprotect acetyl groups. Gratifyingly, applying acetoxyl hydrazinolysis to OA-POSS at 25 °C for 2 h provided OP-POSS in high yield. Fig. 1(A) displays MALDI-TOF mass spectra of OS-POSS, OA-POSS, and OP-POSS, obtained using 2,5-dihydroxybenzoic acid as the matrix. We observe monodisperse mass distributions of the sodiated molecular ions at 1873 g/mol for $[OS\text{-}POSS + Na]^+$, 2337 g/mol for $[OA\text{-}POSS + Na]^+$, and 2001 g/mol for $[OP\text{-}POSS + Na]^+$; the good agreement between the experimental and calculated molecular masses confirms the well-defined structures of OS-POSS, OA-POSS, and OP-POSS. Fig. 1(B) displays ^1H NMR spectra of $Q_8M_8^H$, OS-POSS, OA-POSS, and OP-POSS. The hydrosilylations resulted in the formation of β [$RSiCH_2CH_2R'$] and α [$RSiCH(CH_3)R'$] linkages, where R is the POSS core and R′ is the organic functional group. The molar ratios of β to α linkage were 2.22:1 and 1.82:1 for OS-POSS and OA-POSS, respectively, according to integration of the signals for the protons on the benzylic carbon atoms marked *b* (2H, β-side groups) and *b*′ (1H, α-side groups). Thus, MALDI-TOF mass spectrometry and ^1H NMR spectroscopy confirmed that the POSS products were pure, but comprised several structural isomers.

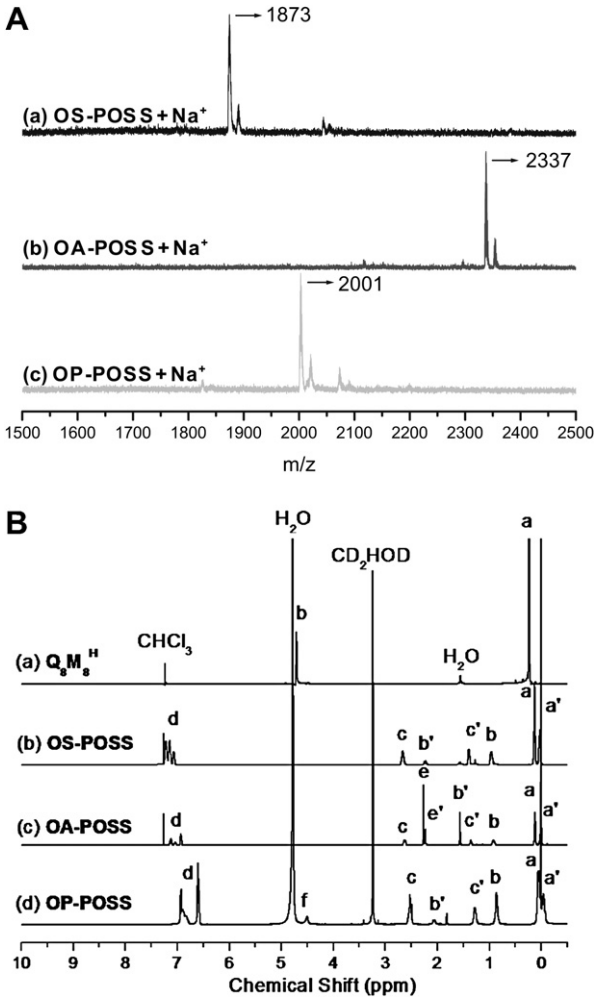

Fig. 1. (A) MALDI-TOF mass spectra of (a) OS-POSS, (b) OA-POSS, and (c) OP-POSS and (B) ^1H NMR spectra of (a) $Q_8M_8^H$, (b) OS-POSS, and (c) OA-POSS in $CDCl_3$ and of (d) OP-POSS in CD_3OD.

3.2. POSS-based polymer nanocomposites

3.2.1. DSC analyses

In general, DSC analysis is one of the most convenient methods for determining the miscibility of blend systems. DSC can determine whether one or two values exist for T_g: a single value of T_g is the most conventionally used criterion for establishing the miscibility of polymer blends; an immiscible polymer blend exhibits more than one value of T_g. The miscibility of most polymer/nanoparticle blend systems has not been studied using DSC because most of these nanoparticles have been inorganic materials that do not display a glass transition at relatively lower temperatures (<400 °C). We obtained conventional second run DSC thermograms of OP-POSS, OA-POSS, OS-POSS, and PEO as shown in Fig. 2; the glass transition temperatures of these pure components were 18, −14, −51, and −45 °C, respectively. Interestingly, even though the molar masses of OP-POSS, OA-POSS, and OS-POSS are only 1978, 2314, and 1850 g/mol, respectively, they displayed single-T_g behavior during the second heating scan. Although pure OP-POSS, OA-POSS, and OS-POSS can be considered as oligomers of poly(vinyl phenol), poly(acetoxystyrene), and polystyrene, respectively, in which the degree of polymerization of the functional POSS derivatives is only 8, their glass transition temperatures are significant lower than those of their corresponding typical high-molecular-weight polymers [47]. Tables 1 and 2 summarizes the thermal properties of these three POSS-related composites.

The melting temperature of the PEO component decreased upon increasing the OP-POSS and OA-POSS contents in the blends, but the addition of OS-POSS did not feature such a linear trend. This phenomenon suggests that the presence of OP-POSS or OA-POSS in the blend hindered the crystallization of PEO—a typical phenomenon for a miscible blend in which the glass transition temperature of the amorphous polymer is higher than that of the crystalline component. In addition, the magnitude of the melting temperature depression of a crystalline polymer blended with an amorphous polymer can reveal important information regarding the miscibility and the polymer–polymer interaction parameter [48]. The melting temperatures of miscible polymer blends are generally depressed for both morphological and thermodynamic reasons. Therefore, we conclude that the relative strength of the interactions of the POSS derivatives with PEO follows the order OP-POSS > OA-POSS.

All of our OP-POSS/PEO and OA-POSS/PEO blends exhibited a single glass transition temperature over the entire blend composition. A single value of T_g strongly suggests that these blends are fully miscible and possess homogeneous amorphous phases. In addition, the values of T_g of the OP-POSS/PEO and OA-POSS/PEO blends shifted to lower temperatures upon increasing their PEO contents. The upturn in the values of T_g at higher PEO contents is due, however, to crystallization of PEO during quenching. This phenomenon suggests not only that crystallization of PEO in the blends can the change the amorphous phase but also that the crystalline PEO can act as a physical cross-linking point that may

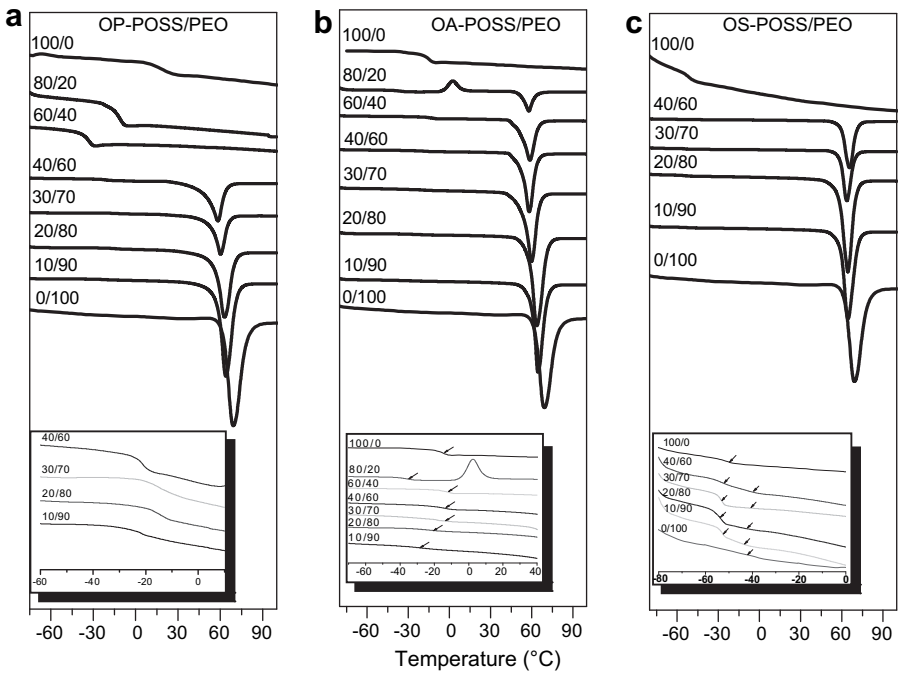

Fig. 2. The DSC scans of PEO blends with different compositions of (a) OP-POSS/PEO (b) OA-POSS/PEO, and (c) OS-POSS/PEO blends.

hinder the molecular mobility of the amorphous phase [49]. The DSC thermograms of the OS-POSS/PEO blends, however, display two values of T_g (see the inset to Fig. 2), implying that they were phase-separated in the amorphous phase. As a result, we conclude that OP-POSS and OA-POSS are miscible with PEO, whereas OS-POSS is not.

3.2.2. DMA analyses

DMA allows the molecular relaxation behavior of small chain segments to be detected and, as a result, the phase heterogeneity can be detected on smaller scales than they can be when using DSC. We performed DMA measurements to further investigate the miscibility of our POSS/PEO blends. The apparently contradictory result between DSC and DMA, in terms of the values of T_g, may be understood by considering the different experimental probe sizes. DMA is capable of identifying compositional heterogeneity on the scale of ca. 5 nm, whereas DSC is sensitive to heterogeneity only on a scale of >20 nm; i.e., heterogeneities on smaller dimensions will be averaged out by this probe [50]. We observed single values of T_g in the DMA analyses of the OP-POSS/PEO and OA-POSS/PEO blends, with a narrow T_g breadth [Fig. 3(a) and (b)]; in contrast, two values of T_g and a broad T_g breadth appeared for the OS-POSS/PEO blend [Fig. 3(c)], indicating that OS-POSS is immiscible with PEO, whereas and OP-POSS and OA-POSS are miscible with it, on the molecular scale—a conclusion that is consistent with our DSC analyses.

3.2.3. TGA analyses

Fig. 4 displays TGA thermograms of OP-POSS, OA-POSS, and OS-POSS and their corresponding blends with PEO. Of these three amorphous POSS derivatives, OP-POSS possesses the highest thermal stability: an onset point at 551 °C (at 20 wt% loss) and a char yield of 68.7 wt%, which is higher than its 51.6 wt% siloxane

Table 1
Thermal properties of OS-POSS, OA-POSS, OP-POSS and PEO used in this study.

Sample	Molar mass	Decomposition		Glass transition	
	Mn (g/mol)[a]	Onset (°C)[b]	Char[c] (wt%)	DSC[d] (°C)	DMA[e] (°C)
OS-POSS	1850	461	38	−51	−49
OA-POSS	2314	443	60	−14	−4
OP-POSS	1978	551	70	18	19
PEO	20000	301	0	−45	−21

[a] Obtained from MALDI-TOF mass spectra.
[b] Recorded at 20 wt% loss.
[c] Obtained from TGA thermograms (heating rate: 20 °C/min).
[d] Obtained from the second run of DSC thermograms (heating rate: 20 °C/min).
[e] Obtained from the first run of DMA analysis (heating rate: 2 °C/min, 1 Hz).

Table 2
Thermal properties of OP-POSS/PEO, OA-POSS/PEO and OS-POSS/PEO blends.

POSS/PEO	T_g (°C)		T_m (°C)	ΔH_m (J/g)	T_d[a] (°C)	Char (wt%)
	DSC	DMA				
Pure PEO	−45.0	−21	68.3	168.3	308.1	0
OP-POSS/PEO						
10/90	−22	−6	63.8	145.6	372.6	7.3
20/80	−14	−9	63.1	120.8	386.2	12.2
30/70	−15	−12	60.2	67.2	390.7	17.2
40/60	−21	−11	58.3	45.1	391.7	24.9
60/40	−33	–	–	–	395.3	36.9
80/20	−11	–	–	–	416.1	48.5
100/0	18	19	–	–	551.0	70.0
OA-POSS/PEO						
10/90	−27	−10	64.6	155.3	378.8	4.2
20/80	−22	−10	63.7	133.2	378.9	8.0
30/70	−19	−1	61.8	108.5	382.6	13.9
40/60	−14	−3	61.1	95.3	387.1	19.3
60/40	−11	–	58.7	66.4	364.4	27.9
80/20	−31	–	58.0	35.0	397.1	44.9
100/0	−14	−4	–	–	442.8	60.0
OS-POSS/PEO						
10/90	−53 −45	−47 −27	64.5	158.6	316.3	8.4
20/80	−53 −47	−47 −27	64.3	134.8	368.1	10.1
30/70	−53 −48	−48 −27	63.7	128.2	383.4	17.3
40/60	−52 −44	−49 −28	65.6	90.8	373.4	18.7
100/0	−51	−49	–	–	461.7	38.0

[a] Obtained from TGA thermograms (20 wt% loss during heating rate: 20 °C/min).

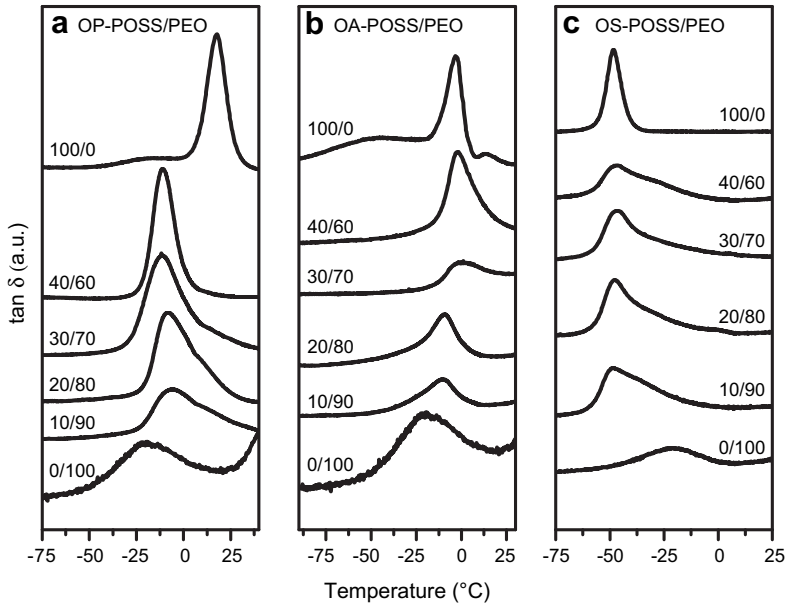

Fig. 3. DMA analyses of PEO blend with different compositions of (a) OP-POSS/PEO (b) OA-POSS/PEO, and (c) OS-POSS/PEO blends.

content. Thus, it appears that decomposition of the organic components of OP-POSS promoted further siloxane degradation, resulting in the higher char yield. OA-POSS and OS-POSS have relatively lower char yields (60.0 and 38.0 wt%, respectively) because their phenol units tend to form aromatic char structures, rather than small molecular vapors, at temperatures above their decomposition temperatures. Degradation of PEO occurs from its chain ends at its decomposition temperature, resulting in low char yields. After incorporating our three POSS derivatives into the PEO matrix, the char yields and decomposition temperatures of these PEO/POSS blends increased upon increasing the POSS content. The decomposition temperatures of the OP-POSS/PEO blends exhibited the most significant increases relative to those of the OA-POSS and OS-POSS composite systems. Furthermore, the char yields of the miscible blends of OP-POSS and OA-POSS with PEO exhibited linearity with respect to the theoretical values, whereas the immiscible OS-POSS/PEO blends did not display any regular trend. In these polymer POSS nanocomposites, the POSS units could evolve into a ceramic superficial layer during the earlier stages of combustion because of the nature of the low surface energy of the siloxane structure of POSS [35]; this ceramic layer would protect the underlying material by limiting heat transfer and hampering the diffusion of oxygen and the evacuation of combustible products, in analogy with the behavior of layered silicates [51,52].

3.2.4. FTIR spectroscopic analyses

Infrared spectroscopy is a highly effective means of investigating specific interactions between polymers. It can be used to study the mechanisms of interpolymer miscibility, through the formation of hydrogen bonds or dipole–dipole interactions, both qualitatively

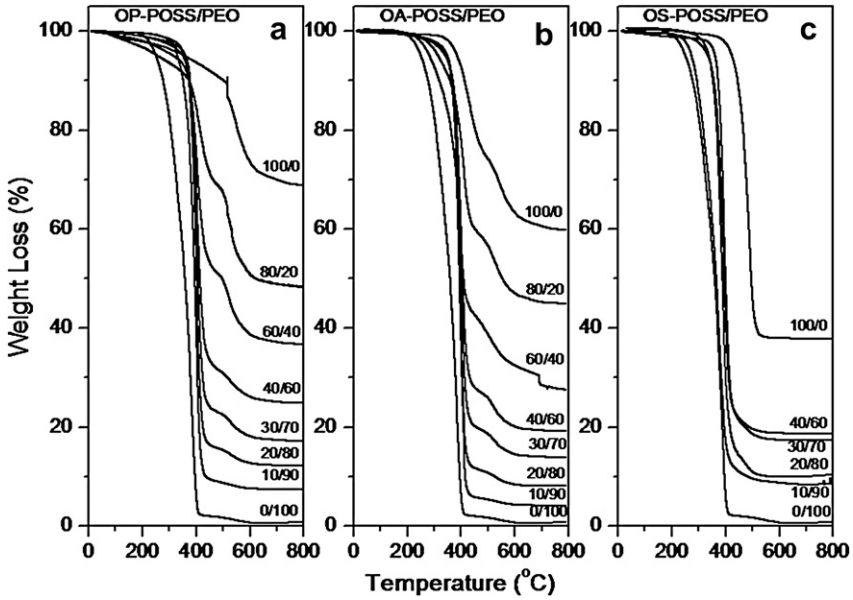

Fig. 4. TGA thermal grams of PEO blend with different compositions of (a) OP-POSS/PEO (b) OA-POSS/PEO, and (c) OS-POSS/PEO blends.

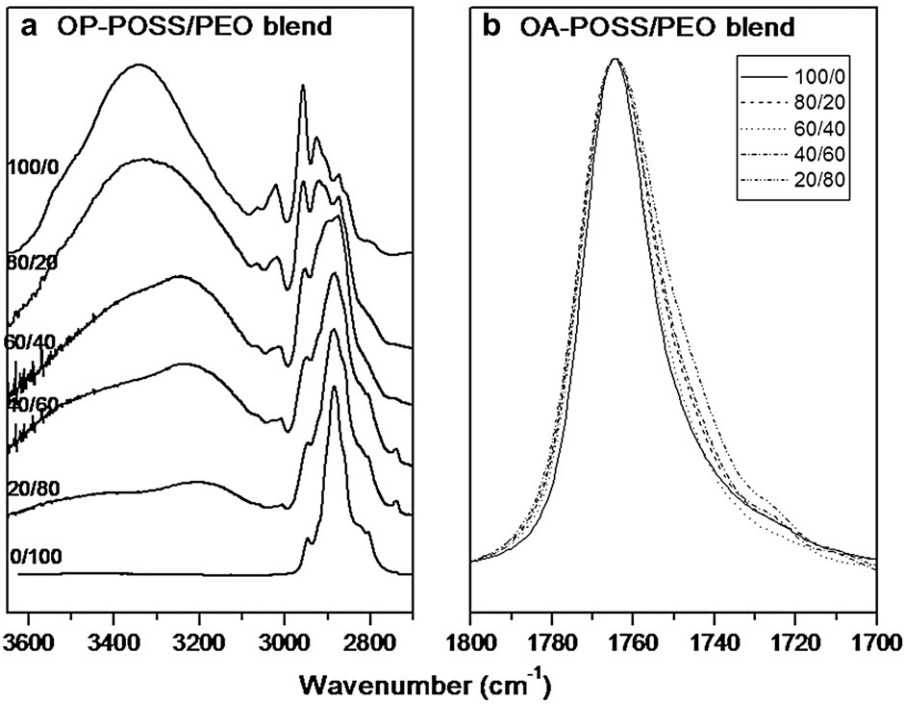

Fig. 5. Infrared spectra of blend of at room temperature in the (a) and hydroxyl stretching of OP-POSS/PEO blend and (b) carbonyl stretching of OA-POSS/PEO blend.

and quantitatively. Here, we discuss only the intermolecular interactions within the OP-POSS/PEO and OA-POSS/PEO blend systems because no specific interactions exist between the OS-POSS and PEO segments. Fig. 5(a) presents scale-expanded IR spectra (2700–4000 cm^{-1}) of various OP-POSS/PEO blends at room temperature. Pure OP-POSS displays two distinct bands in the hydroxyl (OH) stretching region: a broad band centered at 3350 cm^{-1} and a small shoulder at 3525 cm^{-1}, corresponding to the multiply hydrogen bonded and free OH groups, respectively. The peak frequency of the former broad band shifted to lower wavenumber upon increasing the PEO content. Meanwhile, the intensity of the signal of the free OH group decreased gradually—disappearing eventually—upon increasing the PEO content, as expected. This behavior reflects a new distribution of hydrogen bonds, resulting from competition between OH–OH and OH–ether interactions. It also reveals that the OH–ether interactions predominated in PEO-rich blends; therefore, it is reasonable to assign the band at 3200 cm^{-1} as the signal of the OH groups hydrogen bonded to the ether groups. The frequency difference ($\Delta\upsilon$) between the signals for the hydrogen bonded and free OH groups can be used to evaluate the average strength of these intermolecular interactions [53]. Indeed, we calculated that OH–ether inter-association ($\Delta\upsilon = 325\ cm^{-1}$) was stronger than OH–OH self-association ($\Delta\upsilon = 175\ cm^{-1}$) in this system—a result that is consistent with the Painter–Coleman association model prediction [53].

Fig. 5(b) displays scale-expanded IR spectra (1680–1800 cm^{-1}) recorded for neat OA-POSS and various OA-POSS/PEO blends at room temperature. We assign the signal at 1760 cm^{-1} to the absorption of the free carbonyl (C═O) groups of OA-POSS; its half-width increased upon blending with PEO. Therefore, we suspect that weak hydrogen bonding existed between the C═O groups of OA-POSS and the methylene (CH_2) groups of PEO, as we have discussed previously [41]. Fig. 6(a) presents the synchronous 2D correlation maps in the range 1600–3200 cm^{-1}. The bands associated with OA-POSS in this spectral range, at 3037, 2924, 2849, and 1760 cm^{-1}, are due to C–C aromatic, CH, CH_2, and C═O stretching

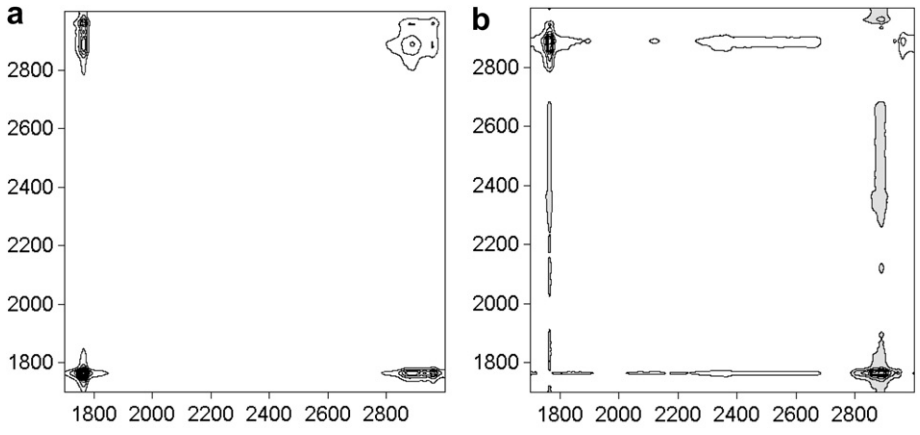

Fig. 6. The synchronous (a) and asynchronous (b) 2D correlation map of OA-POSS/PEO at 1750 cm^{-1}–3000 cm^{-1} region.

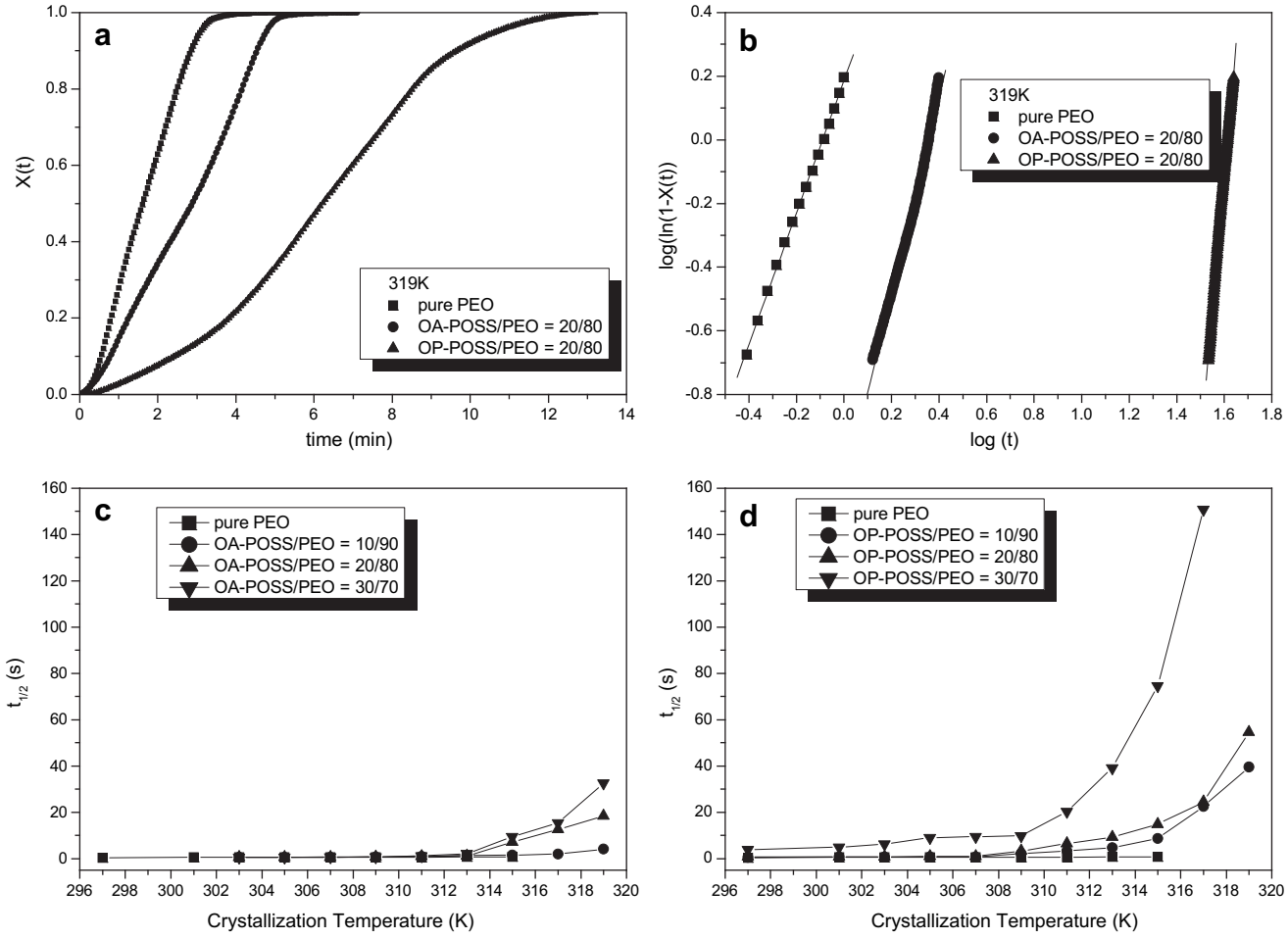

Fig. 7. (a) Crystallization isotherms and (b) Avrami plot at 46 °C for pure PEO, OA-POSS/PEO = 20/80, and OP-POSS/PEO = 20/80. Plots of $t_{1/2}$ versus crystallization temperature of different compositions (c) OA-POSS/PEO and (d) OP-POSS/PEO blends.

vibrations, respectively. The only signal arising from pure PEO appears for CH_2 stretching vibrations at 2884 cm^{-1}. We observe two positive cross-peaks, indicating that the C=O groups of OA-POSS interacted with the CH_2 segments of PEO through weak hydrogen bonds, but with different contributions from various chains. In addition, the asynchronous 2D correlation maps in the range 1700–3200 cm^{-1} [Fig. 6(b)] reveal that these two cross-peaks have opposite phases. Thus, we conclude that the OA-POSS and PEO units were reoriented relative to one another on the molecular level because of C=O groups of OA-POSS interacted with the CH_2 segments of PEO, as depicted in Scheme 2, with the rate of reorientation the CH_2 units of OA-POSS varying with respect to the type of PEO, indicating that two types of microenvironments existed in these binary blend systems. In total, the 2D map reveals that the intensity of the band at 1760 cm^{-1} increased prior to that at 2884 cm^{-1} upon increasing the PEO content [46]. Thus, it appears that dipole–dipole interactions of the C=O groups of OA-POSS existed in the first step and then the C=O groups of OA-POSS interacted with the CH_2 segments of PEO in the second. From these FTIR spectroscopic and DSC analyses, we conclude that the hydrogen bonding interactions between OP-POSS and PEO are stronger than those in the OA-POSS/PEO blend system.

3.2.5. Isothermal crystallization kinetics

Fig. 7(a) displays typical isotherms obtained when plotting relative crystallinity (X_t) against time for pure PEO, OA-POSS/PEO = 20/80, and OP-POSS/PEO = 20/80 at a crystallization temperature of 319 K. The half-time of crystallization ($t_{1/2}$) is defined as the time required for half of the final crystallinity to be developed. We analyzed the crystallization kinetics of the PEO blends using the Avrami treatment [54]:

$$\log[-\ln(1-X_t)] = \log k + n\log(t) \quad (1)$$

where X_t is the weight faction of material crystallized after time t, n is the Avrami exponent (the value of which depends on both the nature of the primary nucleation and the growth geometry of the crystalline entities), and k is the overall kinetic rate constant (which depends on the rates of nucleation and growth). The values of k and n can be calculated from the intercept and slope of Equation (1). Fig. 7(b) reveals that linear relationships exist between $\log[-\ln(1-X_t)]$ and $\log t$ for pure PEO, OA-POSS, and OP-POSS of the same composition at the crystallization temperature of 319 K. Fig. 7(c) and (d) display plots of $t_{1/2}$ versus T_c for the OA-POSS/PEO and OP-POSS/PEO blends. For the sake of brevity, we do not present the values of k, n, and $t_{1/2}$ in this paper, but we note that (i) non-integer values of n occurred in almost all cases resulting from mixed growth or surface nucleation modes and (ii) the values of k decreased upon increasing the content of the hydrogen bond donor and the crystallization temperature. Molecular mobility is the controlling factor at lower crystallization temperatures; at higher crystallization temperatures, the process is controlled by nucleation,

such that k decreases with increasing T_c. Most importantly, these results indicate that the overall crystallization rate decreases in the order OP-POSS/PEO > OA-POSS/PEO, which is consistent with the order of the strength of hydrogen bonding.

3.2.6. Spherulite growth kinetics

The spherulite growth kinetics in miscible blends of crystalline and amorphous polymers has been reported [55]. The Lauritzen–Hoffman theory has been used widely to study the crystallization kinetics in miscible blends of crystalline polymers [56]. In this study, we used a polarizing optical microscope to determine the spherulite growth rates of PEO blends. Fig. 8(a) displays polarized light micrographs of the OA-POSS/PEO = 30/70 blend from the melt at an isothermal temperature T_c of 40 °C for various time intervals. It is clear that the crystal grew with a spherulite morphology. A positive Maltese cross pattern is evident, indicating that the spherulite radius was aligned along or perpendicular to the orientation of the crystalline molecular axis. The dimensions of the crystallites are very sensitive to the crystallization temperature and time. For brevity, Fig. 8(b) presents plots of the spherulite radius versus time only for pure PEO, OA-POSS/PEO = 30/70, and OP-POSS/PEO = 30/70, which were crystallized at 40 °C. The solid lines represent the best least-squares fit to the data. It is clear that a linear increase in the radius occurred with time until the spherulite impinged on others, with the slopes of the lines increasing in the order pure PEO > OA-POSS/PEO > OP-POSS/PEO. Fig. 8(c) and (d) display the dependence of G on T_c for pure PEO and various OA-POSS/PEO and OP-POSS/PEO blends; they indicate that the spherulite growth rate decreased upon increasing the content of the hydrogen bond-donating POSS at a given value of T_c. The presence in the blends of hydrogen-bonding POSS having higher values of T_g significantly decreased the rate of PEO crystallization, as expected. Furthermore, the reduction in the spherulite growth rate also decreased upon increasing the crystallization temperature. Similarly, these results also indicate that the spherulite growth rate decreased in the order OP-POSS/PEO > OA-POSS/PEO, again consistent with the order of hydrogen bonding strength. In general, there are three main factors dictating the depression of the crystallization rate in miscible crystalline polymers: (i) a decrease in the segmental mobility of the crystalline polymer transporting across the liquid–solid interface because of the higher value of T_g of the blends, (ii) a dilution effect that reduces the number of crystallizable segments at the surface of the growing spherulite, and (iii) a decrease in supercooling resulting from the depression in the melting point [57].

The interaction energy density parameters, calculated from the melting depression of PEO using the Nishi–Wang equation [48], followed the order OP-POSS/PEO > OA-POSS/PEO, implying that the degree of supercooling was inversely proportional to the hydrogen bonding strength at a constant crystallization

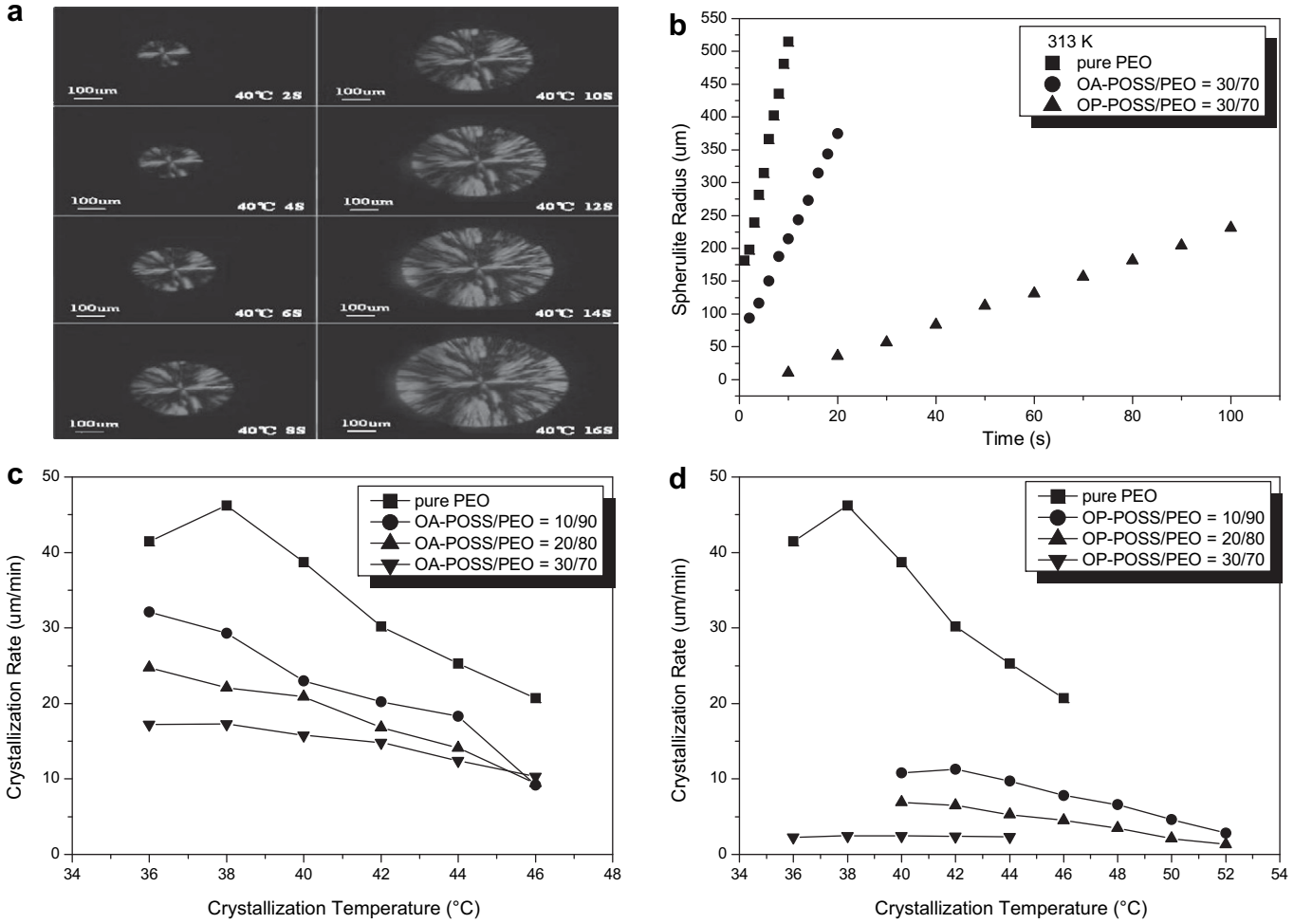

Fig. 8. (a) Polarized light micrographs of OA-POSS/PEO = 30/70 blend at 46 °C for various times, (b) radius of spherulite as a function of time at 46 °C for pure PEO, OA-POSS/PEO = 30/70, and OP-POSS/PEO = 30/70, and radial growth rate (G) as a function of T_c for (c) OA-POSS/PEO and (d) OP-POSS blends.

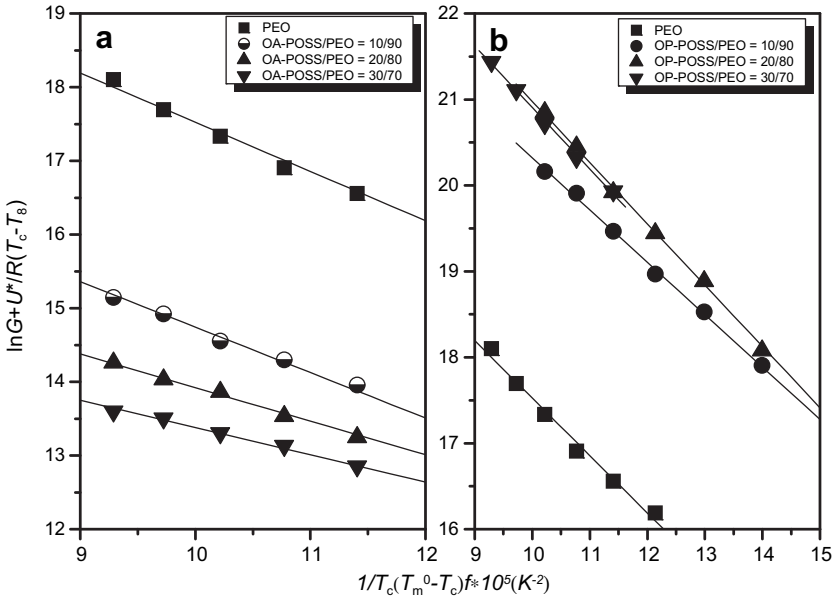

Fig. 9. Kinetics analysis of crystallization rate constant data employing WLF constants for (a) OA-POSS/PEO and (b) OP-POSS/PEO blends.

temperature. Therefore, the crystallization rate depression we observed in this study is consistent with the degree of supercooling. Nonetheless, Wang and Jiang [58] found that the dependence of the decrease in the crystallization growth rate on the glass transition temperature in SAN/PCL blends dominated over the polymer–polymer interaction parameter based on the Flory–Huggins theory. The glass transition temperatures of the OP-POSS/PEO and OA-POSS/PEO blend systems were almost identical, suggesting that they did not play the main role in determining the crystallization kinetics in these two blends featuring hydrogen bonding interactions. Therefore, it seems that the hydrogen bonding strength or the polymer–polymer interaction parameter is more important than the chain mobility in hydrogen bonded PEO blend systems.

The Lauritzen–Hoffman model, described below, can be used to analyze the spherulite crystallization behavior of homopolymers and some crystalline/amorphous polymer blends. We used it to analyze the spherulite crystallization behavior of PEO blends. The equation is

$$G = G_0 \exp\left[\frac{-U^*}{R(T-T_\infty)}\right]\exp\left[\frac{-K_g}{fT\Delta T}\right] \quad (2)$$

where G_0 is the front factor, U^* is the activation energy for the segment diffusion to the site of crystallization, R is the gas constant, T_∞ is the hypothetical temperature below which all viscous flow ceases, K_g is the nucleation parameter, $\triangle T$ is the degree of supercooling (equal to $T_m^0 - T_c$), and f is a correction factor [equal to $2T_c/(T_m^0 + T_c)$]. We treated the parameters U^* and T_∞ as variables to maximize the quality of the fit to Equation (2). In this study, we used the Williams–Landel–Ferry (WLF) values of U^* (4120 cal/mol) and T_∞ ($T_g = 51.6$) [59]. The nucleation parameter K_g is given by [60]

$$K_g = \frac{nb\sigma\sigma_e T_m^0}{\Delta h_f k_B} \quad (3)$$

where b is the thickness of a monomolecular layer, σ is the lateral surface free energy, σ_e is the surface free energy of chain folding, Δh_f is the heat of fusion per unit volume, T_m^0 is the equilibrium melting temperature, and k_B is the Boltzmann constant. Typically, the value of n is 4 in regimes I and III, but 2 in regime II. Often, it is most convenient to rearrange Equation (2) as

$$\ln G + \frac{U^*}{R(T-T_\infty)} = \ln G_0 - \frac{K_g}{T(\Delta T)f} \quad (4)$$

A plot of the left-hand side of Equation (4) versus $1/T_c(\Delta T)f$ gives a line having a slope equal to $-K_g$. Figs. 9(a) and 9(b) display the growth rate data for pure PEO and OA-POSS/PEO and OP-POSS/PEO blends of various compositions, plotted according to Equation (4). Table 3 summarizes the values of K_g obtained from Fig. 9. In this study, we assign the regime to be regime III at ca. 40–50 °C [26]. The derived value of K_g can be used to calculated σ_e and the work of chain folding q for PEO, employing a thickness b of 0.465 nm [61], the value of T_m^0 of 72.9 °C determined in our previous study [49], and a value of Δh_f of 2.13×10^9 erg/cm^3 [61]. The lateral surface free energy σ may be estimated by the Thomas–Stavely relationship [62]:

$$\sigma = \alpha b_0 \left(\Delta h_f\right) \quad (5)$$

where α is an empirical constant, usually assumed to be 0.1 for vinyl polymers and 0.25 for high-melting polyesters [63]. Because a low melting point polymer, such as PEO, has a long run of CH_2 groups, much like PE, a value of 0.1 is recommended. We obtained a value of σ_e for pure PEO of 30.67 erg/cm^2, which agrees well with the value reported previously [60].

Table 3 also lists the values of K_g(III) and σ_e for various blend compositions. Both values increased upon increasing the content of OA-POSS, indicating that the ability of PEO to crystallize increased accordingly. Similar decreases in surface free energy of chain folding

Table 3
Comparison of K_g and surface free energies of chain folding for OA-POSS/PEO and OP-POSS/PEO blends.

OA-POSS/PEO	K_g (III) $\times 10^{-4}$ (deg^2)	σ_e (erg/cm^2)	OP-POSS/PEO	K_g (III) $\times 10^{-4}$ (deg^2)	σ_e (erg/cm^2)
0/100	6.68	30.7	0/100	6.68	30.7
10/90	6.17	28.4	10/90	6.20	28.5
20/80	4.55	20.9	20/80	7.13	32.8
30/70	3.69	17.0	30/70	7.16	33.0

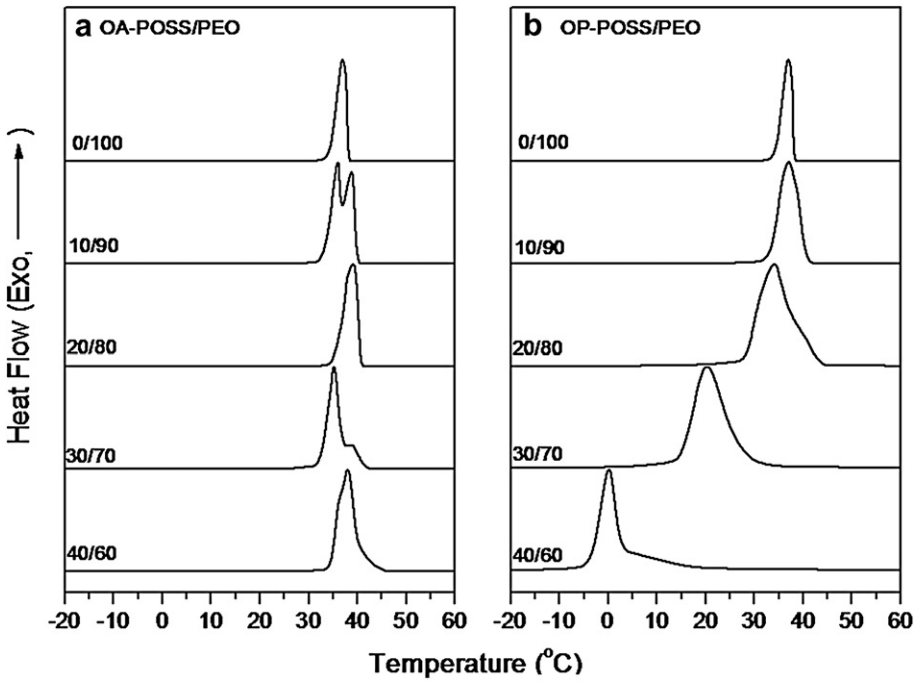

Fig. 10. The DSC scans of (a) OA-POSS/PEO and (b) OP-POSS/PEO blends with different composition at cooling rate −5 °C/min from 100 to −50 °C.

have also been observed for PAS/PEO and PBzMA/PEO blend systems upon increasing their PAS and PBzMA contents, respectively [41,64]. This result indicates that the amorphous component of the OA-POSS reduces the surface free energy of chain folding and provides the driving force for the crystallization of PEO. Note, however, that the surface free energy of chain folding decreases only upon increasing the OP-POSS content up to OP-POSS/PEO = 10/90; from that point on it increased—a phenomenon that has also been observed in phenolic/PEO, phenolic/PCL [65], and PVPh/PCL blend systems. In a previous study [57], we found that if the inter-association equilibrium constant is larger than the self-association equilibrium constant, the surface free energy in the polymer blend is larger than that in the pure crystalline homopolymer—as in the case for phenolic/PCL, PVPh/PCL, and phenolic/PEO [64] blend systems, which are similar to the OP-POSS/PEO blend system because the OH–ether interaction between OP-POSS and PEO is stronger than the self-association OH–OH interactions of OP-POSS. Conversely, the surface free energy in polymer blends having a relatively weaker interaction is smaller than that in the pure crystalline homopolymer, as in the case for PVC/PCL [57], SAN/PCL [57], PAS/PEO [41], and PMA/PHB [57] blends—a phenomenon that we also observed in our OA-POSS/PEO blend system. A recent theoretical model has predicted [66] that a miscible blend of polymers featuring a relatively large difference in T_g, and exhibiting weak intermolecular interactions will exhibit two dynamic microenvironments: one near the mean blend mobility and the other close to that of the component having the lower value of T_g. In our 2D FTIR spectroscopic analysis above, we observed two cross-peaks having an opposite order of intensity, indicating that the micro phase separation occurs as a result of two different motions in this binary OA-POSS/PEO blend. The amorphous component of AS-POSS may play a role as a nucleation agent to reduce the surface free energy of chain folding and provide the driving force for the crystallization of PEO.

Fig. 10 presents the DSC thermograms of pure PEO and the OA-POSS/PEO and OP-POSS/PEO binary blends, recorded using a slowcooling rate (5 °C/min) to determine the crystallization temperature. The crystallization temperature of the OA-POSS/PEO blend in Fig. 10(a) is relatively high and it displays a small crystallization peak, which is also higher than that of the virgin PEO, an indication of fast nucleation due to the OA-POSS nanoparticles behaving as nucleating agents [67]; this behavior has also been observed in PP/POSS composites [68]. Beck reported that a good nucleation agent can decrease the value of σ_e [69]. A foreign surface can decrease the nucleus size required for crystal growth because the creation of an interface between the polymer crystal and the substrate may be less hindered than the creation of the corresponding free polymer crystal surface. The grafting of AS-functionalized POSS nanoparticles in the PEO main chain can lead to a better dispersion of POSS nanoparticles in the PEO matrix, thereby decreasing the work required to create a new surface. In addition, the crystallization temperatures of the OP-POSS/PEO binary blends underwent an initial increase and then decrease upon increasing the OP-POSS content, which shows a similar trend with σ_e. This result reveals that the OP-POSS units could penetrate into the lamellar regions of the PEO matrix. Therefore, we can consider that this binary OP-POSS/PEO blend is miscible in its amorphous phase. In this blend system features strong hydrogen bonding, the surface free energy of chain folding increases upon increasing the content of OP-POSS. This behavior is probably related to the fact that, during crystallization, OP-POSS may readily form physical cross-links with PEO molecules, thereby favoring the formation of large loops on the surface of the PEO lamellar crystals [70]. Thus, the surface enthalpy term overwhelms the surface entropy of chain folding because of the presence of strong hydrogen bonding between the OP-POSS and PEO units.

4. Conclusions

We have prepared three polymer-like amorphous POSS derivatives—OS-POSS, OA-POSS, and OP-POSS—through hydrosilylation. The intermolecular interactions between these POSS derivatives and PEO segments have a great effect on the thermal properties and miscibility behavior of their blends. The strongest hydrogen bonding interactions occurred between OP-POSS and PEO; as such,

their blend displayed superior thermal properties. The addition of an amorphous hydrogen-bonding POSS nanoparticle into PEO depressed the rates of both overall crystallization and spherulite growth—to a greater extent with OP-POSS/PEO than with OA-POSS/PEO, consistent with the relative intermolecular hydrogen bonding strengths.

Acknowledgment

This work was supported financially by the National Science Council, Taiwan, Republic of China, under Contract No. NSC 97-2221-E-110-013-MY3 and NSC 97-2120-M-009-003. The authors would like to thank Dr. Chu-Hua Lu and Professor Feng-Chih Chang of Department of Applied Chemistry, National Chiao-Tung University in Taiwan for their help in synthesizing in OS-POSS, OA-POSS, and OP-POSS.

References

[1] Giannelis EP. Adv Mater 1996;8:29.
[2] Vo LT, Giannelis EP. Macromolecules 2007;40:8271.
[3] Bansal A, Yang H, Li C, Benicewicz BC, Kumar SM, Schadler LS. J Polym Sci Polym Phys 2006;44:2944.
[4] Xu H, Kuo SW, Lee JS, Chang FC. Macromolecules 2002;35:8788.
[5] Li GZ, Wang LC, Ni HL, Pittman CU. J Inorg Organometal Polym 2001;11:123.
[6] Phillips SH, Haddad TS, Tomczak SJ. Current Opin Solid State Mater Sci 2004;8:21.
[7] Joshi M, Butola BS. J Macromol Sci Polym Rev 2004;C44:389.
[8] Mark JE. Acc Chem Res 2004;37:946.
[9] Pielichowaski K, Niuguna J, Janowski B, Pielichowski J. Adv Polym Sci 2006;201:225.
[10] Lickiss PD, Rataboul F. Adv Organmetal Chem 2008;57:1.
[11] Kuo SW, Lee HF, Huang WJ, Jeong KU, Chang FC. Macromolecules 2009;42:1619.
[12] Mather PT, Jeon HG, Romo-Uribe A, Haddad TS, Lichtenhan JD. Macromolecules 1999;32:1194.
[13] Zhang C, Laine RM. J Am Chem Soc 2000;122:6979.
[14] Zheng L, Farris RJ, Coughlin EB. Macromolecules 2001;34:8034.
[15] Li GZ, Wang L, Toghiani H, Daulton TL, Koyama K, Pittman U. Macromolecules 2001;34:8686.
[16] Kim KM, Chujo Y. J Polym Sci Polym Chem 2001;39:4035.
[17] Lu CH, Kuo SW, Huang CF, Chang FC. J Phys Chem C 2009;113:3517.
[18] Kuo SW, Wu YC, Lu CH, Chang FC. J Polym Sci Polym Phys 2009;17:811.
[19] Kim KM, Keum DK, Chujo Y. Macromolecules 2003;36:867.
[20] Sellinger A, Laine RM. Macromolecules 1996;29:2327.
[21] Xu H, Kuo SW, Lee JS, Chang FC. Polymer 2002;43:5117.
[22] Lee YJ, Kuo SW, Huang WJ, Lee HY, Chang FC. J Polym Sci Polym Phys 2004;42:1127.
[23] Kuo SW, Lin HC, Huang WJ, Huang CF, Chang FC. J Polym Sci Polym Phys 2006;44:673.
[24] Yen YJ, Kuo SW, Huang CF, Chen JK, Chang FC. J Phys Chem B 2008;112:10821.
[25] Huang CF, Kuo SW, Lin FJ, Huang WJ, Wang CF, Chen WY, et al. Macromolecules 2006;39:300.
[26] Sheen YC, Lu CH, Huang CF, Kuo SW, Chang FC. Polymer 2008;49:4017.
[27] Wu J, Haddad TS, Mather PT. Macromolecules 2009;42:1142.
[28] Chan SC, Kuo SW, Chang FC. Macromolecules 2005;38:3099.
[29] Liu YH, Yang XT, Zhang WA, Zheng SX. Polymer 2006;47:6814.
[30] Lee YJ, Huang JM, Kuo SW, Chang FC. Polymer 2005;46:10056.
[31] Maitra P, Wunder SL. Chem Mater 2002;14:4494.
[32] Kim BS, Mather PT. Macromolecules 2002;35:8378.
[33] Zhang C, Bunning TJ, Laine RM. Chem Mater 2001;13:3653.
[34] Lee YJ, Huang JM, Kuo SW, Lu JS, Chang FC. Polymer 2005;46:173.
[35] Lin HC, Kuo SW, Huang CF, Chang FC. Macromol Rapid Commun 2006;27:537.
[36] Espi E, Iruin JJ. Macromolecules 1991;24:6458.
[37] Jiang M, Li M, Zhou H. Adv Polym Sci 1999;146:121.
[38] Sawatari C, Kondo T. Macromolecules 1999;32:1949.
[39] Kuo SW, Liu WP, Chang FC. Macromol Chem Phys 2005;206:2307.
[40] Kuo SW, Lin CL, Chang FC. Macromolecules 2002;35:278.
[41] Kuo SW, Huang WJ, Huang CF, Chan SC, Chang FC. Macromolecules 2004;37:4164.
[42] Wastlund C, Maurer FHJ. Macromolecules 1997;30:5870.
[43] Chen X, An L, Yin J, Sun Z. Macromolecules 1999;32:5905.
[44] Feldstein MM, Shandryuk GA, Kuptsov SA, Plate NA. Polymer 2000;41:5327.
[45] Noda I. J Am Chem Soc 1989;111:8116.
[46] Noda I, Ozaki Y. Two-dimensional correlation spectroscopy. John Wiley & Sons; 2004.
[47] O'Driscoll K, Sanayei RA. Macromolecules 1991;24:4479.
[48] Nishi T, Wang TT. Macromolecules 1975;8:909.
[49] Kuo SW, Chang FC. Macromolecules 2001;34:4089.
[50] Kuo SW, Huang CF, Tung PH, Huang WJ, Huang JM, Chang FC. Polymer 2005;46:9348.
[51] Fu HK, Huang CF, Kuo SW, Lin HC, Yei DR, Chang FC. Macromol Rapid Commun 2008;29:1216.
[52] Fu HK, Kuo SW, Yeh DR, Chang FC. J Nanomater 2008:739613.
[53] Coleman MM, Graf JF, Painter PC. Specific interactions and the miscibility of polymer blends, Lancaster, PA; 1991.
[54] Avrami M. J Chem Phys 1939;7:1103.
[55] Wang TT, Nishi T. Macromolecules 1977;10:4219.
[56] Hoffman JD, Davis GT, Lauritzen JI. In: Hannay NB, editor. Treatise on solid state chemistry, vol. 3. New York: Plenum Press; 1976.
[57] Kuo SW, Chan SC, Chang FC. Macromolecules 2003;36:6653.
[58] Wang Z, Jiang B. Macromolecules 1997;30:6223.
[59] Williams ML, Landel RF, Ferry JD. J Am Chem Soc 1975;77:3701.
[60] Hoffman JD. Polymer 1983;24:3.
[61] Godovsky YK, Slonimsky GL, Garbar NM. J Polym Sci C 1972;38:1.
[62] Thomas DG, Staveley LAK. J Chem Soc 1952:4569.
[63] Alfonso GC, Russell TP. Macromolecules 1986;19:1143.
[64] Mandal TK, Kuo JF, Woo EM. J Polym Sci Polym Phys 2000;38:562.
[65] Kuo SW, Chan SC, Chang FC. J Polym Sci Polym Phys 2004;42:117.
[66] Kumar SK, Colby RH, Anastasiadis H, Fytas G. J Chem Phys 1996;105:3777.
[67] Fina A, Tabunai D, Frache A, Camino G. Polymer 2005;46:7855.
[68] Zhou Z, Cui L, Zhang Y, Zhang Y, Yin N. J Polym Sci Polym Phys 2008;46:1762.
[69] Beck HN. J Appl Polym Sci 1975;19:371.
[70] Zhong Z, Guo Q. J Polym Sci Polym Phys 1999;37:2726.